

Giant negative terahertz photoconductivity in controllably doped carbon nanotube networks

Maria G. Burdanova,^{*,†} Alexey P. Tsapenko,[‡] Daria A. Satco,[‡] Reza Kashtiban,[†]
Connor D. W. Mosley,[†] Maurizio Monti,[†] Michael Staniforth,[†] Jeremy Sloan,[†]
Yuriy G. Gladush,[‡] Albert G. Nasibulin,^{‡,¶} and James Lloyd-Hughes^{*,†}

[†]*University of Warwick, Department of Physics, Gibbet Hill Road, Coventry, CV4 7AL,
United Kingdom.*

[‡]*Skolkovo Institute of Science and Technology, Nobel str. 3, 121205 Moscow, Russian
Federation.*

[¶]*Aalto University, Department of Applied Physics, Puumiehenkuja 2, 00076 Espoo, Finland*

E-mail: m.burdanova@warwick.ac.uk; j.lloyd-hughes@warwick.ac.uk

Abstract

A strong negative photoconductivity was identified in thin film networks of single-walled carbon nanotubes using optical pump, THz probe spectroscopy. The films were controllably doped, using either adsorption doping with different p-type dopant concentrations, or ambipolar doping using an ionic gate. While doping enhanced the THz conductivity and increased the momentum scattering rate, interband photoexcitation lowered the spectral weight and reduced the momentum scattering rate. This negative THz photoconductivity was observed for all doping levels, regardless of the chemical potential, and decayed within a few picoseconds. The strong many-body interactions inherent to these 1D conductors led to trion formation under photoexcitation, lowering

the overall conductivity of the carbon nanotube network. The large amplitude of negative THz photoconductivity and the tunability of its recovery time with doping offer promise for spectrally wide-band ultrafast devices including THz detectors, polarizers and modulators.

Keywords

carbon nanotubes; terahertz spectroscopy; negative photoconductivity.

The functionality of single-walled carbon nanotubes (SWCNTs) in device applications¹⁻⁴ is underpinned by their unique optical and electronic properties, such as 1D ballistic conduction, large exciton binding energies and strong many-body interactions.^{5,6} The local conductivity of an individual SWCNT can be extremely high, and changes with its chirality, defect density, and chemical environment.^{7,8} The overall macroscopic conductivity of a carbon nanotube thin-film network is dependent upon the local conductivity of each SWCNT backbone, as well as the network's connectivity and any energetic barriers at tube-tube contacts.⁹⁻¹¹ Terahertz (THz) radiation provides a non-contact probe of the local motion of charges in nanomaterials and nanocomposites,^{12,13} which has been exploited to explore the plasmonic nature of charge transport in SWCNT thin films.¹⁴⁻¹⁷ Expanding our knowledge of the optical and THz response of charge carriers in carbon nanotubes is vital for their use in nanoelectronics, as well as for the plethora of emerging THz devices based on SWCNTs, which include sources, detectors, polarizers and modulators.^{18,19} In particular, these applications require high charge mobilities, picosecond switching times and strong optical absorption, for instance to achieve high modulation depths in optically-switched THz modulators.

Excitons are the primary photo-product in SWCNTs at room temperature,^{6,20} because of the strong, weakly-screened Coulomb interaction between holes and electrons. This yields large binding energies for excitons in both semiconducting²⁰ and metallic²¹ nanotubes, and strong optical absorption. Further, excited states below the lowest (E_{11}) singlet exciton

state have been observed in hole-doped SWCNTs, which were assigned to the formation of trions (charged excitons).²² Trion formation requires an exciton to bind with another charge, provided either by doping or from the dissociation of another exciton. Evidence for trions in SWCNTs has been provided from absorption,²³ photoluminescence,^{24,25} time-resolved photoluminescence²⁶ and pump-probe spectroscopy^{26–28} experiments. Hole doping is thought to promote trion formation by creating a relaxation channel from bright excitons to trions consisting of a dark exciton and a charge.²⁹

The ultrafast energy and charge transfer processes that follow the pulsed excitation of excitons have been studied by transient absorption spectroscopy in the visible and infrared,^{6,30–32} while changes in the THz conductivity have been observed using optical-pump terahertz-probe (OPTP) spectroscopy.^{33–39} While some studies of the THz photo-response have reported free-carrier generation in metallic and semiconducting films, assigned to the dissociation of optically generated excitons,³⁴ others have observed resonances in the THz photoconductivity spectra which have been assigned to intra-excitonic transitions.^{36,38} A plasmonic THz response peaked at 4 THz was observed by Kampfrath *et al.*, which lowered in amplitude under photoexcitation.³⁵ Recently, Karlsen *et al.* studied the THz conductivity of thin films of long and short SWCNTs, and attributed a photoinduced reduction in the THz conductivity to a broadening of the plasmonic response, assuming that photoexcitation heats the SWCNTs and increases the momentum scattering rate.³⁹ Kar and Sood reported the terahertz photoconductivity of single-walled and double-walled carbon nanotubes and interpreted the photoconductivity using Boltzmann transport theory for free charges only, ignoring the equilibrium plasmonic contribution.⁴⁰

The above experiments highlight challenges in understanding the optical and THz response of carbon nanotubes. These studies involved a wide range of SWCNT films with different morphologies (e.g. surfactant^{34,38} or polymer wrapped³⁶), chiralities (semiconducting SWCNTs, metallic SWCNTs, or both), different physical lengths,³⁹ and varying SWCNT densities. However the influence of doping on the THz photoconductivity, and the interaction

between trions, excitons and equilibrium charges, has remained unexplored.

In this work, we report a strong negative THz photoconductivity in thin-films of single-walled carbon nanotubes (SWCNTs) with controlled doping levels. The equilibrium conductivity and negative photoconductivity of adsorption-doped and electrically-gated samples were examined, in order to distinguish properties observed due to doping from any electromagnetic response of the adsorbed nanoparticles. Negative THz photoconductivity is found to be an intrinsic property of these conductive SWCNT thin films, whereby the mobile carrier density was reduced, or the carrier mass enhanced, by photoexcitation. The strong many-body interactions in 1D SWCNTs led to a reduction in the number of delocalized, mobile charges by the formation of trions. The high THz conductivity of the films was efficiently modulated by the strong optical absorption of the SWCNTs, giving high modulation depths while retaining a picosecond response time. Further, the dynamic response time was tuned by changing the doping level. This suggests the promise of controllably-doped SWCNTs for ultrafast nanoelectronic devices, including THz modulators and detectors.

Results and Discussion

Influence of adsorption doping or ionic gating on equilibrium UV-THz optical properties. We synthesized SWCNT films via the floating-catalyst aerosol CVD method,⁴¹ creating 40 nm-thick SWCNT films comprising an extended network of individual and bundled (around 5 per bundle) SWCNTs. A mean diameter of 2.1 nm was determined from transmission electron microscopy of a number of individual tubes (a typical nanotube is shown in Figure 1(a) inset), while tube lengths were above 10 μm . As-deposited films were used in order to avoid additional processing steps (such as sonication and surfactant wrapping) which can introduce additional defects, change the chemical and dielectric environment, and reduce the length of the as-grown SWCNTs. Hence, the films contained a mix of one-third metallic and two-thirds semiconducting SWCNTs, as expected theoretically,⁵ and

as found previously in films grown under similar conditions, using TEM to establish CNT chiralities. A substantial amount of prior work on doped SWCNTs used films containing large bundles, where adsorption doping at the surface will not work effectively for the central tubes in the bundle; hence increasing attention has focused upon the doping of individual SWCNTs or small bundles.^{42,43} Here the small number of SWCNTs per bundle permitted effective p-type doping at different levels using HAuCl_4 solutions with varying concentrations, while electrostatic doping permitted ambipolar doping of films made from the as-deposited SWCNTs (see Methods).

The absorption spectra of the pristine SWCNT films [blue line in Figure 1(a)] show three absorption peaks in the near infrared range, corresponding to the E_{11}^S (2300 nm), E_{22}^S (1300 nm) and E_{11}^M (890 nm) excitonic absorption lines for interband transitions in semiconducting (S) and metallic (M) SWCNTs. At longer wavelengths the absorbance rises monotonically through the infrared towards the THz range, as a result of free carrier absorption by axial plasmon motion and delocalized carriers.^{16,44}

In Figure 1(c) the conductivity can be seen to increase towards zero frequency, indicating the prevalence of delocalized charge transport over a long length scale in these films. The equilibrium conductivity of SWCNT films is well described by the Drude plus plasmon model (solid lines),^{16,44} where some fraction of free charges undergo a plasmon resonance, representing the confined collective motion of carriers along tubes, while other charges undergo a Drude-like free carrier response, indicative of delocalized intertube transport along percolating channels on a larger scale. Details of the fitting model are provided in the Supplemental Information. When SWCNTs form an extended network, a strong Drude contribution can result,^{44–47} while a plasmon response is expected for isolated tubes. The plasmon frequency is given by $\omega_{\text{pl}} = v_{\text{Q}}\pi/L$ for a plasmon with speed v_{Q} confined to move in a length L .^{15,44} When $L \simeq 1\text{ }\mu\text{m}$, the plasmon frequency falls in the THz range at $\omega_{\text{pl}}/2\pi \simeq 3\text{ THz}$.^{17,44} For the longer SWCNT studied herein ($L \geq 10\text{ }\mu\text{m}$), the fitted plasmon frequency is lower, at $\omega_{\text{pl}}/2\pi = 0.15\text{ THz}$. This yields $v_{\text{Q}} \simeq 3 \times 10^6\text{ ms}^{-1}$, assuming $L \simeq 10\text{ }\mu\text{m}$, consistent with

estimates from theory,¹⁵ although we stress that v_Q may be lower if the actual L is lower. In the fit a constant ω_{pl} was assumed for all cases, as samples were derived from the same growth and hence had the same physical length L . Previous studies found that ω_{pl} depends sensitively on the length of the CNTs¹⁷ and does not vary substantially with carrier density when doped¹⁷ or when photoexcited.³⁵

A large change in absorbance occurs upon increasing adsorption doping [red, green and black lines in Figure 1(a)]. For the lowest concentration (4 mM, red) the chemical potential has lowered, depleting the two highest valence bands of electrons, suppressing the E_{11}^S and E_{22}^S excitonic optical absorption transitions.^{48,49} From the absence of E_{22}^S at 0.95 eV and the presence of E_{11}^M at 1.4 eV we deduced the chemical potential $\mu \simeq -0.6$ eV from $-E_{11}^M/2 < \mu < -E_{22}^S/2$. The reported p-type doping under HAuCl_4 ⁵⁰ was confirmed by Raman spectra of the G mode, shown in Figure 1(b). The conductivity in the THz range is increased by doping, as for instance shown for the 15 mM HAuCl_4 sample in Figure 1(d). At higher doping levels additional visible absorption peaks arose between 1000 nm and 2000 nm [green and black lines in Fig. 1(a)], which can be attributed to intersubband transitions like E_{31}^S .^{49,51,52}

In the ultraviolet, the increase in the absorbance after adsorption doping may be explained by the SWCNTs' π -plasmon mode changing strength, similarly to the case reported for Fe-doped SWCNTs.⁵³ These new peaks disappeared within 6 months (Supplementary Information) because of the de-doping processes whereby chlorine ions detach from the SWCNTs slowly.^{54,55} Additional absorption around 550 nm occurs due to the surface plasmon mode of gold nanoparticles, as can be seen in the de-doped sample (Supplementary Information). These features were not observed in the gated samples.

The Raman-active G mode can be used as a sensitive probe of the magnitude and type of doping. In Figure 2 a systematic shift of the G mode's peak due to p-type doping can be seen from $\Delta\nu = 2 \text{ cm}^{-1}$ for the lowest doping, to $\Delta\nu = 18 \text{ cm}^{-1}$ for the highest doping.⁵⁰ A shift in the G mode for the gated sample is also evident: applying a gate voltage $V_g = -2 \text{ V}$ resulted in $\Delta\nu = 2.5 \text{ cm}^{-1}$, similar to the lightest doped sample, while n-type doping was

obtained with positive gate voltage in this device.

Terahertz conductivity and photoconductivity. The THz conductivity of the films in equilibrium, $\sigma_{\text{eq}}(\omega)$, and at times t after photoexcitation, $\sigma(\omega, t)$, were determined for all doped samples, and as a function of voltage for the ionic gate devices. The optical pump wavelength was 650 nm, and the fluence F was varied up to $F = 26 \mu\text{J}/\text{cm}^{-2}$ in the results reported herein. In all cases, the amplitude of the transmitted THz pulse was *increased* under optical excitation, demonstrating negative photoconductivity. This is in contrast to the normal positive photoconductivity of semiconductors such as GaAs (Supplemental Information).

In optical-pump, THz-probe spectroscopy the pump-induced change in the THz electric field transmitted through a sample is measured at different pump-probe delays, i.e. $\Delta E/E = (E_{\text{on}} - E_{\text{off}})/E_{\text{off}}$. Here we analyzed the THz conductivity versus probe frequency at different pump-probe delays, $\sigma(\omega, t) = \sigma_{\text{eq}}(\omega) + \Delta\sigma(\omega, t)$. It is important to analyze the total conductivity of the SWCNT film, rather than just the photoconductivity, as photoexcited quasiparticles can alter the behavior of the charges present in equilibrium. We introduce an expression for the photoconductivity of a thin-film which is valid for a heavily doped film, and for large transmission changes:

$$\Delta\sigma = \frac{-\frac{\Delta E}{E} \left[\frac{(n_i + n_k)c\epsilon_0}{d} - i\omega\epsilon_0(n_i n_k + n_{\text{off}}^2) \right]}{1 + \frac{\Delta E}{E}} - i\epsilon_0\Delta\epsilon_L\omega, \quad (1)$$

where d is the film thickness (40 nm), and n_i and n_k are the complex refractive indices of the media on either side of the film, and all conductivities are complex, e.g. $\sigma = \sigma_1 + i\sigma_2$. This expression includes a change in the lattice component of the dielectric function after photoexcitation, $\Delta\epsilon_L$, which can arise because the pump bleaches the excitonic interband transition strength. The complex refractive index of the film before photoexcitation, n_{off} , was obtained from the equilibrium THz transmission measurements. Equation 1 is derived and described in more detail in the Supplemental Information. In contrast, the widely-used

expression⁵⁶ $\Delta\sigma = -(n_i + n_k)c\epsilon_0(\Delta E/E)/d$ is not valid in this case as it is not accurate at large $\Delta E/E$, nor for films with a high equilibrium conductivity. In the limit of small $\Delta E/E$, low equilibrium conductivity, and no photoinduced change in the high-frequency dielectric constant ($\Delta\epsilon_L = 0$), Equation 1 reduces to this simpler form. For the free-standing pristine and doped films, $n_i = n_k = 1.0$, while for the ionic gel-gated, quartz-encapsulated device we assumed $n_i = n_k = 2.0$.

A prominent negative photoconductivity can be seen in Figure 3 by comparing the real part of the sheet conductance σd of the undoped film without excitation (open blue circles) and 2 ps after photoexcitation at several pump fluences (filled blue circles). The observed conductivity after photoexcitation was lower in amplitude, and an enhanced suppression of $\sigma_1(\omega, t = 2 \text{ ps})$ with increasing fluence is evident in Figure 3(a). A higher fluence resulted in a progressively narrower $\sigma_1(\omega, t = 2 \text{ ps})$, as can be seen for instance from the frequency f_{HWHM} at which the conductivity is half its maximum value (red squares). At later pump-probe delays, the conductivity recovered rapidly back towards its equilibrium level, increasing in amplitude and broadening in width, as shown in Figure 3(b). The solid lines show fits using the Drude plus plasmon model (Supplemental Information)

The influence of free charges, provided by adsorption doping or electrostatic gating, on the negative THz photoconductivity is reported in Fig. 4. For all doping levels photoexcitation lowers the conductivity of the film, with an overall spectral shape consistent with long-range transport from delocalized charges. The electrostatically gated sample [Fig. 4(c)] shows the same behaviour as samples doped with HAuCl_4 . Therefore, the THz spectroscopy results are sensitive to the doping of the SWCNTs, rather than being linked to the electromagnetic response of the adsorbed nanoparticles. Superimposed upon this low-frequency peak to $\sigma_1(\omega, t = 2 \text{ ps})$ are small resonances at 0.9 THz and 1.7 THz (marked by asterisks in Fig. 4), which are not seen in the pristine $\sigma_1(\omega, t)$ spectra after excitation in Fig. 3. These peaks may be linked to intra-excitonic transitions associated with dark excitons: Luo *et al.* observed a peak in σ_1 at 1.5 THz for (6,5) SWCNTs.³⁸ Given their low overall spectral weight we

do not consider them further here. Note also that f_{HWHM} of the electrically-gated sample is marginally larger than the adsorption-doped sample, which may be a consequence of increased scattering associated with short-range disorder in the local dielectric environment of the ionic gel.

Origin of negative photoconductivity. Negative photoconductivity is rare for semiconductors and semi-metals, and previously was reported for 2D materials such as graphene and MoS₂.⁵⁷ In graphene it can be explained by changes to the Drude weight resulting from thermal broadening of the carrier distribution after optical excitation: the momentum scattering rate increases, lowering the Drude weight, and outweighing the increase in carrier density.^{58,59} Recently, Karlsen *et al.* studied the negative THz photoconductivity in thin films of undoped, long, 2 nm diameter SWCNTs.³⁹ The photoinduced reduction in THz conductivity was attributed to a broadening of the plasmonic response, for a plasmon at low frequency (10 GHz), where photoexcitation was assumed to heat free charges and thereby *increase* the momentum scattering rate, assuming that the number of charges remains constant. Here, in contrast, we find that photoexcitation produces a pronounced *reduction* in the scattering rate, evident from the narrowing of $\sigma_1(\omega)$, simultaneously to a reduction in mobile carrier density.

Within the Drude model of intraband free-carrier absorption, $\sigma(\omega) = \sigma_D/(1 - i\omega\tau_D)$, where $\sigma_D = Ne^2\tau_D/m^*$ for carrier density N , momentum scattering time τ_D and effective mass m^* . Hence, $f_{\text{HWHM}} = 1/(2\pi\tau_D)$ and the observed reduction in f_{HWHM} under photoexcitation implies an increase in momentum scattering time (reduction in momentum scattering rate). The experimental negative photoconductivity reported here corresponds to an overall reduction in the height of the peak, σ_D , as a consequence of a reduction in N , or an increase in m^* . Importantly, the change in N or m^* after photoexcitation must outweigh the increase in τ_D , which acts in the opposite direction, to increase σ_D . While stated here with reference to the Drude model, we stress that similar conclusions can be drawn for the plasmon model in the limit $\omega \gg \omega_{\text{pl}}$.

To analyse the change in spectral weight with doping and photoexcitation, and in a model-independent manner, we used the partial sum rule for the effective electron density,^{60,61} N_{eff} , defined by

$$N_{\text{eff}}(\omega') = \frac{2m^*m_e}{\pi e^2} \int_0^{\omega'} \sigma_1(\omega) d\omega, \quad (2)$$

where $\omega'/2\pi = 2.2 \text{ THz}$ is a cut-off frequency, m_e is the free space electron mass, and m^* is the carrier effective mass. $N_{\text{eff}}(\omega')$ is the effective density of charges contributing to electromagnetic absorption at frequencies below ω' . As m^* is not known a priori, and changes with doping level, we report N_{eff}/m^* in Figure 5(a) for the pristine SWCNT film and the 15 mM AuCl_4 -doped film. In both cases photoexcitation lowers the spectral weight N_{eff}/m^* calculated from the sum rule, indicating either a reduction in N_{eff} or an increase in m^* after the optical pump is absorbed.

Under photoexcitation, an exciton in a SWCNT can bind to a free charge to form a trion. As a bound state of three charges, trions have a larger effective mass, and hence lower carrier mobility and conductivity than free charges. For trion formation to be possible, there must be (i) a large trion binding energy, and (ii) a free charge within the exciton diffusion length (the distance it can travel on average before recombination), which can exceed 100 nm in SWCNTs.^{6,62–64} The first condition is evidently satisfied: trions lay lower in energy than the bright singlet exciton E_{11} transition by 70 meV for suspended SWCNTs.⁶⁵ To assess the second condition, we calculated the number of excitons and free charges per SWCNT as follows.^{28,66} From the pump fluence ($26 \mu\text{Jcm}^{-2}$ at 650 nm) and absorbance we estimated that the exciton sheet density was $1.7 \times 10^{13} \text{ cm}^{-2}$, assuming one photon absorbed produces one exciton. From transmission electron microscopy the SWCNT areal density was $2.5 \times 10^{11} \text{ cm}^{-2}$, and the ratio of these sheet densities yields 70 excitons per SWCNT.

The sum rule analysis provides the carrier sheet density in equilibrium, which varies from $2.4 \times 10^{14} \text{ cm}^{-2}$ for the pristine sample to $1.2 \times 10^{15} \text{ cm}^{-2}$ for the highest adsorption doping case, corresponding to between 1000 and 5000 free charges per SWCNT (assuming $m^* = 1$). However, if a lower effective mass⁶⁷ more typical of these tubes is assumed ($m^* = 0.2$) then

between 200 and 1000 free charges per SWCNT results. Assuming an average SWCNT length of $1\mu\text{m}$, the hole density per unit length is between 1 and 5 nm^{-1} for the highest p-type doped sample. This is comparable to the number of dopant ions per unit length.⁵⁰ Since the exciton and hole number density are both high, there is a ready supply of free charges close to each exciton on each SWCNT, satisfying condition (ii).

The momentum scattering rate, as tracked by f_{HWHM} in Figure 5(b), lowers with increasing fluence. Indeed, $f_{\text{HWHM}} \propto N_{\text{eff}}$ [inset in Fig. 5(b)], demonstrating that the momentum scattering rate increases with N_{eff} for each sample. Single-particle transport has been well studied in SWCNTs: carrier scattering from disorder, impurities, interactions with the substrate, electron-hole scattering and electron-phonon scattering have been widely discussed.⁵ Acoustic phonon and impurity scattering mechanisms dominate the total scattering rate for low energy carriers at room temperature, while optical and zone-boundary phonon emission becomes possible for carriers with energies above 160 meV .^{47,66,68} However, the conductivity of charges including any interactions with excitons, and the conductivity of trions, have not been investigated theoretically to the best of our knowledge. We provide two possible explanations for the observed narrowing in $\sigma_1(\omega, t)$: (1) that the formation of trions reduces the free hole density, lowering the momentum scattering rate of the remaining holes; (2) the residual conductivity observed under photoexcitation may represent the delocalized Drude or plasmonic response of the metallic SWCNTs present in our films (1/3 of tubes), assuming that the contribution of the semiconducting tubes is efficiently suppressed. This second suggestion is based on the observation that metallic SWCNTs are less sensitive to short range disorder than semiconducting SWCNTs,^{5,69} and hence have lower momentum scattering rates.

Influence of doping on recombination dynamics. To further elucidate the origin of negative photoconductivity (positive $\Delta E/E$), we obtained N_{eff}/m^* and f_{HWHM} from $\sigma_1(\omega, t)$ spectra at pump-probe delays from $t = -2.5\text{ ps}$ to $t = 17.5\text{ ps}$, as reported in Figure 6 for the 15 mM doped sample and the pristine SWCNT film at a fluence of $26\mu\text{Jcm}^{-2}$. At zero pump-

probe delay, N_{eff}/m^* is rapidly suppressed for both the doped and pristine samples. The larger relative reduction in N_{eff}/m^* for the doped sample is a result of its higher absorbance at the pump wavelength [Fig. 2]. After zero pump-probe delay, N_{eff}/m^* recovers rapidly towards its equilibrium level. The solid lines illustrate fits using $N_{\text{eff}}/m^*(t) = A - Be^{-t/\tau}$, where A is the equilibrium value of N_{eff}/m^* and B is the modulation depth. The recombination times obtained are $\tau = 2.4$ ps for the pristine SWCNT film and $\tau = 1.5$ ps for the doped film. A similar reduction in τ for increasing p-type doping was observed for the gated device. These numbers are close to the 2.7 ps single-exponential trion lifetime reported for hole-doped SWCNTs.^{29,70} Trions in polymer-wrapped (6,5) semiconducting SWCNTs were shown to be formed within 500 fs of photoexcitation by rapid exciton diffusion to less-mobile holes, before subsequently decaying with a 2 ps lifetime.²⁸ The recovery times observed here are therefore consistent with trion decay times, which are similar to exciton lifetimes.

The momentum scattering rate is also modified dynamically during the recombination process, lowering after photoexcitation and recovering with the same timescale as N_{eff}/m^* , as illustrated in Fig. 6(b). As with the fluence-dependent data, $f_{\text{HWHM}} \propto N_{\text{eff}}/m^*$ [inset in Fig. 6(c)]. The doped sample has a shallower gradient than the pristine sample, implying that the carrier scattering rate is a function of the chemical potential.

Also shown in Figure 6(c) is $\Delta E(t)/E$ obtained at the peak of the THz pulse, for different pump-probe delays t . The photoinduced THz modulation depth exceeds $\Delta E(t)/E = +60\%$ for the pristine sample when pumped at fluence $F = 26 \mu\text{Jcm}^{-2}$. This suggests a potential application of the giant negative photoconductivity of SWCNTs in ultrafast THz modulators. This modulation depth exceeds those previously obtained from positive photoconductivity in GaAs nanowires ($\Delta E(t)/E = -15\%$ for 14 stacked and co-aligned layers, $F = 280 \mu\text{Jcm}^{-2}$)⁷¹ and polymer-wrapped SWCNTs ($\Delta E(t)/E < -0.2\%$, $F = 175 \mu\text{Jcm}^{-2}$).⁷² The modulation depth for negative photoconductivity in our SWCNT films is larger than that for MoS₂ ($\Delta E/E = 1.5\%$, $F = 50 \mu\text{Jcm}^{-2}$)⁷³ and graphene ($\Delta E/E = 3\%$, $F = 50 \mu\text{Jcm}^{-2}$).⁷⁴ Here, the high THz conductivity of the films was efficiently modulated by the strong optical absorp-

tion of the SWCNTs, giving high modulation depths while retaining an ultrafast decay time, which was tuned by changing the doping level. At higher fluences the changes in N_{eff}/m^* , f_{HWHM} and $\Delta E/E$ [Fig. 5(c)] appear to saturate, potentially as a result of the bleaching of the excitonic absorption resulting in less than one exciton on average per incident photon.

Conclusions

We examined negative THz photoconductivity and its recovery dynamics in p-type chemically doped films, achieved using HAuCl_4 , and in electrically-gated devices made with an ionic gel. The relatively small number of SWCNTs per bundle resulted in efficient control of the chemical potential and doping level by either method, in comparison to larger bundles where changing the chemical potential of the central SWCNTs is harder. We correlated the ultrafast THz spectroscopy study with results from UV-vis-IR absorption spectroscopy, Raman spectroscopy, and transmission electron microscopy, allowing a full characterization of the film’s morphology and optoelectronic properties.

The observation of negative photoconductivity for pristine SWCNT films, adsorption doped films and under ionic gating demonstrates that this is an intrinsic property of SWCNT thin films, and that it occurs for all chemical potentials. This behaviour is in contrast to the previously observed gate-tuned photoconductivity in graphene,⁷⁵ where negative photoconductivity was observed at high chemical potential and attributed to an increased momentum scattering rate. Here, the high THz equilibrium conductivity was attributed to the high mobility and long conductivity length of these films, as well as effective doping. The negative photoconductivity effect observed was created by a photoinduced lowering of the free charge density (or increased mass), which we ascribed to the formation of trions, and which simultaneously lowered the momentum scattering rate. Future work may systematically examine negative photoconductivity in aligned SWCNTs with precisely constrained lengths and controlled network connectivity, to better disentangle the plasmonic, Drude-like and

intra-excitonic features.

This improved understanding of the transient transport dynamics of photoexcited carriers in carbon nanotubes is important in the drive towards nanoelectronics and THz devices built on SWCNTs. Finally, the negative ultrafast photoconductivity reported here offers significantly larger modulation depths (reaching $\Delta E/E > 60\%$) than obtained at the same pump fluences in alternative materials, opening new prospects for the design of ultrafast spectrally wide-band THz modulators, polarizers, emitters and detectors. Long CNTs grown by aerosol CVD are ideal candidates for these applications as they show giant modulation depth, broad bandwidth, and picosecond switching times that can be tuned by doping.

Methods

Sample preparation. A dry transfer technique was used to make free-standing films with a size 1 cm x 1 cm x 40 nm.⁴¹ As-grown films were used, which contained the catalytic Fe nanoparticles used in CVD growth. TEM images showed that these Fe nanoparticles were encapsulated by layers of carbon. To chemically dope, pristine SWCNT films were spin-coated at 1000 rpm using a droplet of HAuCl_4 ethanol solution of a certain concentration, which was varied in the range from 4 to 30 mM. After 20 s the solvent had completely evaporated. Samples were stored in air and measured over a period of weeks to 6 months after doping.

For electrical gating, SWCNT films from the same growth as used in the adsorption doping study were transferred using the dry-transfer technique onto a 2 mm-thick z-quartz substrate, with edges touching a gold contact. A drop of the ionic gel 1-Butyl-3-methylimidazolium hexafluorophosphate covered the SWCNT film and connected to a lateral gold gate contact. A second identical z-quartz substrate was placed on top, and sealed by epoxy, to encapsulate the devices, preventing moisture and oxygen from interacting with the ionic gel or SWCNTs. The ionic gel was stable over the entire duration of the experiments, as confirmed by regular

voltammograms (current-voltage loops) and repeated UV-visible absorbance measurements.

Spectroscopic techniques. Equilibrium absorbance spectra were determined via THz time-domain spectroscopy (0.12-4 THz range), Fourier-transform infrared spectroscopy (3-200 THz), and a UV/VIS/NIR spectrophotometer (200-1200 THz, or 250-1500 nm in wavelength). Raman spectra using a confocal micro-spectrometer (Labram, Jobin-Yvon Horiba) with a 660 nm laser at 0.58 mW (with spectral resolution 1 cm^{-1} and spatial resolution $1.5\text{ }\mu\text{m}$). The high quality of the pristine SWCNT films was confirmed by the low D mode intensity in comparison to the G mode, which was a factor of 120 more intense.^{50,76}

The optical pump beam in the OPTP measurements was created by an optical parametric amplifier (TOPAS), seeded with a 1 kHz, 40 fs, 800 nm pulse (from a Newport Spectra Physics Spitfire ACE) to create pulses with a tunable centre wavelength. The THz probe pulse was generated using a 2 mm-thick $\langle 110 \rangle$ GaP crystal, and detected with electro-optic sampling in a 2.0 mm-thick $\langle 110 \rangle$ ZnTe crystal. The THz beam was $< 0.5\text{ mm}$ in diameter at the sample due to the high numerical aperture off-axis parabolic mirrors, while the optical pump beam was more than 3 times larger in diameter. The THz generation beam was chopped at 500 Hz while the optical pump beam was chopped at 250 Hz. The fastest observable dynamic for this spectrometer was observed to be around 200 fs for the photoconductivity rise time of GaAs.⁷⁷ All THz experiments were carried out in the transmission geometry in a nitrogen environment and at room temperature. The choice of 2mm-thick quartz for the gated devices meant that the THz spectral resolution was not reduced substantially in comparison to the THz spectral resolution for the spectrometer, set by the 2mm-thick crystals.

Notes

The authors declare no competing financial interest. Data related to this publication is available from the University of Warwick data archive at <http://wrap.warwick.ac.uk/114910>.

Acknowledgments

The UK authors would like to thank the EPSRC (UK) for support under grants EP/N010825/1, EP/M010643/1 and EP/R019428/1. MGB would like to thank the Russian Government for financial support (Global Education program). DAS, YGG and AGN acknowledge the Russian Science Foundation (Project 17-19-01787), and APT acknowledges RFBR (Project 18-32-00246), for partial financial support.

Associated content

Supporting information: Transmission Electron Microscopy; Verifying negative and positive photoconductivity; Thin film transmission expression; Fitting parameters; Fluence-dependent THz differential transmission; Additional features in conductivity spectra of doped nanotubes; Degradation of a control sample.

References

1. Guldi, D. M.; Rahman, G. M. A.; Prato, M.; Jux, N.; Qin, S.; Ford, W. Single-Wall Carbon Nanotubes as Integrative Building Blocks for Solar-Energy Conversion. *Angewandte Chemie International Edition* **2005**, *44*, 2015–2018.
2. Barone, P. W.; Baik, S.; Heller, D. A.; Strano, M. S. Near-infrared optical sensors based on single-walled carbon nanotubes. *Nature Materials* **2005**, *4*, 86–92.
3. De Volder, M. F. L.; Tawfick, S. H.; Baughman, R. H.; Hart, A. J. Carbon Nanotubes: Present and Future Commercial Applications. *Science (New York, N.Y.)* **2013**, *339*, 535–539.
4. Suzuki, D.; Oda, S.; Kawano, Y. A Flexible and Wearable Terahertz Scanner. *Nature Photonics* **2016**, *10*, 809–813.

5. Ilani, S.; McEuen, P. L. Electron Transport in Carbon Nanotubes. *Annual Review of Condensed Matter Physics* **2010**, *1*, 1–12.
6. Amori, A. R.; Hou, Z.; Krauss, T. D. Excitons in Single-Walled Carbon Nanotubes and Their Dynamics. *Annual Review of Physical Chemistry* **2018**, *69*, 81–99.
7. Mustonen, K.; Susi, T.; Kaskela, A.; Laiho, P.; Tian, Y.; Nasibulin, A. G.; Kauppinen, E. I. Influence of the Diameter of Single-Walled Carbon Nanotube Bundles on the Optoelectronic Performance of Dry-Deposited Thin Films. *Beilstein Journal of Nanotechnology* **2012**, *3*, 692–702.
8. Senga, R.; Pichler, T.; Yomogida, Y.; Tanaka, T.; Kataura, H.; Suenaga, K. Direct Proof of a Defect-Modulated Gap Transition in Semiconducting Nanotubes. *Nano Letters* **2018**, *18*, 3920–3925.
9. Ozel, T.; Gaur, A.; Rogers, J. A.; Shim, M. Polymer Electrolyte Gating of Carbon Nanotube Network Transistors. *Nano Letters* **2005**, *5*, 905–911.
10. Blackburn, J. L.; Barnes, T. M.; Beard, M. C.; Kim, Y.-H.; Tenent, R. C.; McDonald, T. J.; To, B.; Coutts, T. J.; Heben, M. J. Transparent Conductive Single-Walled Carbon Nanotube Networks with Precisely Tunable Ratios of Semiconducting and Metallic Nanotubes. *ACS Nano* **2008**, *2*, 1266–1274.
11. Bârsan, O. A.; Hoffmann, G. G.; van der Ven, L. G.; de With, G. Single-Walled Carbon Nanotube Networks: The Influence of Individual Tube-Tube Contacts on the Large-Scale Conductivity of Polymer Composites. *Advanced Functional Materials* **2016**, *26*, 4377–4385.
12. Ulbricht, R.; Hendry, E.; Shan, J.; Heinz, T. F.; Bonn, M. Carrier Dynamics in Semiconductors Studied With Time-Resolved Terahertz Spectroscopy. *Reviews of Modern Physics* **2011**, *83*, 543–586.

13. Lloyd-Hughes, J.; Jeon, T. I. A Review of the Terahertz Conductivity of Bulk and Nano-Materials. *Journal of Infrared, Millimeter, and Terahertz Waves* **2012**, *33*, 871–925.
14. Akima, N.; Iwasa, Y.; Brown, S.; Barbour, A. M.; Cao, J. B.; Musfeldt, J. L.; Matsui, H.; Toyota, N.; Shiraishi, M.; Shimoda, H. *et al.* Strong anisotropy in the far-infrared absorption spectra of stretch-aligned single-walled carbon nanotubes. *Adv. Mater.* **2006**, *18*, 1166.
15. Nakanishi, T.; Ando, T. Optical Response of Finite-Length Carbon Nanotubes. *Journal of the Physical Society of Japan* **2009**, *78*, 114708.
16. Zhang, Q.; H  roz, E. H.; Jin, Z.; Ren, L.; Wang, X.; Arvidson, R. S.; L  ttge, A.; Kono, J. Plasmonic Nature of the Terahertz Conductivity Peak in Single-Wall Carbon Nanotubes. *Nano Letters* **2013**, *13*, 5991–5996.
17. Morimoto, T.; Joung, S.-K.; Saito, T.; Futaba, D. N.; Hata, K.; Okazaki, T. Length-Dependent Plasmon Resonance in Single-Walled Carbon Nanotubes. *ACS Nano* **2014**, *8*, 9897–9904.
18. Hartmann, R. R.; Kono, J.; Portnoi, M. E. Terahertz Science and Technology of Carbon Nanomaterials. *Nanotechnology* **2014**, *25*, 322001.
19. Wang, R.; Xie, L.; Hameed, S.; Wang, C.; Ying, Y. Mechanisms and Applications of Carbon Nanotubes in Terahertz Devices: A Review. *Carbon* **2018**, *132*, 42–58.
20. Wang, F.; Dukovic, G.; Brus, L. E.; Heinz, T. F. The Optical Resonances in Carbon Nanotubes Arise From Excitons. *Science* **2005**, *308*, 838–841.
21. Wang, F.; Cho, D. J.; Kessler, B.; Deslippe, J.; Schuck, P. J.; Louie, S. G.; Zettl, A.; Heinz, T. F.; Shen, Y. R. Observation of Excitons in One-Dimensional Metallic Single-Walled Carbon Nanotubes. *Physical Review Letters* **2007**, *99*, 227401.

22. Matsunaga, R.; Matsuda, K.; Kanemitsu, Y. Observation of Charged Excitons in Hole-doped Carbon Nanotubes Using Photoluminescence and Absorption Spectroscopy. *Physical Review Letters* **2011**, *106*, 037404.
23. Hartleb, H.; Späth, F.; Hertel, T. Evidence for Strong Electronic Correlations in the Spectra of Gate-Doped Single-Wall Carbon Nanotubes. *ACS Nano* **2015**, *9*, 10461–10470.
24. Park, J. S.; Hirana, Y.; Mouri, S.; Miyauchi, Y.; Nakashima, N.; Matsuda, K. Observation of Negative and Positive Trions in the Electrochemically Carrier-Doped Single-Walled Carbon Nanotubes. *Journal of the American Chemical Society* **2012**, *134*, 14461–14466.
25. Mouri, S.; Miyauchi, Y.; Iwamura, M.; Matsuda, K. Temperature Dependence of Photoluminescence Spectra in Hole-Doped Single-Walled Carbon Nanotubes: Implications of Trion Localization. *Physical Review B - Condensed Matter and Materials Physics* **2013**, *87*, 045408.
26. Koyama, T.; Shimizu, S.; Miyata, Y.; Shinohara, H.; Nakamura, A. Ultrafast Formation and Decay Dynamics of Trions in P-Doped Single-Walled Carbon Nanotubes. *Physical Review B - Condensed Matter and Materials Physics* **2013**, *87*, 165430.
27. Yuma, B.; Berciaud, S.; Besbas, J.; Shaver, J.; Santos, S.; Ghosh, S.; Weisman, R. B.; Cognet, L.; Gallart, M.; Ziegler, M. *et al.* Biexciton, Single Carrier, and Trion Generation Dynamics in Single-Walled Carbon Nanotubes. *Physical Review B - Condensed Matter and Materials Physics* **2013**, *87*, 205412.
28. Bai, Y.; Olivier, J.-H.; Bullard, G.; Liu, C.; Therien, M. J. Dynamics Of Charged Excitons in Electronically and Morphologically Homogeneous Single-Walled Carbon Nanotubes. *Proceedings of the National Academy of Sciences of the United States of America* **2018**, *115*, 674–679.

29. Nishihara, T.; Yamada, Y.; Okano, M.; Kanemitsu, Y. Trion Formation and Recombination Dynamics in Hole-Doped Single-Walled Carbon Nanotubes. *Applied Physics Letters* **2013**, *103*, 023101.
30. Wang, J.; Graham, M. W.; Ma, Y.; Fleming, G. R.; Kaindl, R. A. Ultrafast spectroscopy of midinfrared internal exciton transitions in separated single-walled carbon nanotubes. *Physical Review Letters* **2010**, *104*, 177401.
31. Santos, S. M.; Yuma, B.; Berciaud, S.; Shaver, J.; Gallart, M.; Gilliot, P.; Cognet, L.; Lounis, B. All-Optical Trion Generation in Single-Walled Carbon Nanotubes. *Physical Review Letters* **2011**, *107*, 187401.
32. Graham, M. W.; Chmeliov, J.; Ma, Y.-Z.; Shinohara, H.; Green, A. A.; Hersam, M. C.; Valkunas, L.; Fleming, G. R. Exciton Dynamics in Semiconducting Carbon Nanotubes. *The Journal of Physical Chemistry B* **2011**, *115*, 5201–5211.
33. Perfetti, L.; Kampfrath, T.; Schapper, F.; Hagen, A.; Hertel, T.; Aguirre, C. M.; Desjardins, P.; Martel, R.; Frischkorn, C.; Wolf, M. Ultrafast Dynamics of Delocalized and Localized Electrons in Carbon Nanotubes. *Physical Review Letters* **2006**, *96*, 027401.
34. Beard, M. C.; Blackburn, J. L.; Heben, M. J. Photogenerated Free Carrier Dynamics in Metal and Semiconductor Single-Walled Carbon Nanotube Films. *Nano Letters* **2008**, *8*, 4238–4242.
35. Kampfrath, T.; Von Volkman, K.; Aguirre, C. M.; Desjardins, P.; Martel, R.; Krenz, M.; Frischkorn, C.; Wolf, M.; Perfetti, L. Mechanism of the Far-Infrared Absorption of Carbon-Nanotube Films. *Physical Review Letters* **2008**, *101*, 267403.
36. Xu, X.; Chuang, K.; Nicholas, R. J.; Johnston, M. B.; Herz, L. M. Terahertz Excitonic Response of Isolated Single-Walled Carbon Nanotubes. *Journal of Physical Chemistry C* **2009**, *113*, 18106–18109.

37. Jensen, S. A.; Ulbricht, R.; Narita, A.; Feng, X.; Müllen, K.; Hertel, T.; Turchinovich, D.; Bonn, M. Ultrafast Photoconductivity of Graphene Nanoribbons and carbon Nanotubes. *Nano Letters* **2013**, *13*, 5925–5930.
38. Luo, L.; Chatzakis, I.; Patz, A.; Wang, J. Ultrafast Terahertz Probes of Interacting Dark Excitons in Chirality-Specific Semiconducting Single-Walled Carbon Nanotubes. *Physical Review Letters* **2015**, *114*, 107402.
39. Karlsen, P.; Shuba, M. V.; Kuzhir, P. P.; Nasibulin, A. G.; Lamberti, P.; Hendry, E. Sign Inversion in the Terahertz Photoconductivity of Single-Walled Carbon Nanotube Films. *Physical Review B* **2018**, *98*, 241404.
40. Kar, S.; Sood, A. Ultrafast Terahertz Photoresponse of Single and Double - Walled Carbon Nanotubes: Optical Pump-Terahertz Probe Spectroscopy. *Carbon* **2019**, *144*, 731 – 736.
41. Nasibulin, A. G.; Moisala, A.; Brown, D. P.; Jiang, H.; Kauppinen, E. I. A Novel Aerosol Method for Single Walled Carbon Nanotube Synthesis. *Chemical Physics Letters* **2005**, *402*, 227–232.
42. Kalbac, M.; Farhat, H.; Kavan, L.; Kong, J.; Sasaki, K. I.; Saito, R.; Dresselhaus, M. S. Electrochemical Charging of Individual Single-Walled Carbon Nanotubes. *ACS Nano* **2009**, *3*, 2320–2328.
43. Paolucci, D.; Franco, M. M.; Iurlo, M.; Marcaccio, M.; Prato, M.; Zerbetto, F.; Pénicaud, A.; Paolucci, F. Singling Out the Electrochemistry of Individual Single-Walled Carbon Nanotubes in Solution. *Journal of the American Chemical Society* **2008**, *130*, 7393–7399.
44. Shao, D.; Yotprayoonsak, P.; Saunajoki, V.; Ahlskog, M.; Virtanen, J.; Kangas, V.; Volodin, A.; Haesendonck, C. V.; Burdanova, M.; Mosley, C. D. *et al.* Conduction Prop-

- erties of Thin Films From a Water Soluble Carbon Nanotube/Hemicellulose Complex. *Nanotechnology* **2018**, *29*, 145203.
45. Zhukova, E. S.; Grebenko, A. K.; Bubis, A. V.; Prokhorov, A. S.; Belyanchikov, M. A.; Tsapenko, A. P.; Gilshteyn, E. P.; Kopylova, D. S.; Gladush, Y. G.; Anisimov, A. S. *et al.* Terahertz-Infrared Electrodynamics of Single-Wall Carbon Nanotube Films. *Nanotechnology* **2017**, *28*, 445204.
 46. Gorshunov, B. P.; Zhukova, E. S.; Starovatykh, J. S.; Belyanchikov, M. A.; Grebenko, A. K.; Bubis, A. V.; Tsebro, V. I.; Tonkikh, A. A.; Rybkovskiy, D. V.; Nasibulin, A. G. *et al.* Terahertz Spectroscopy of Charge Transport in Films of Pristine and Doped Single-Wall Carbon Nanotubes. *Carbon* **2018**, *126*, 544–551.
 47. Karlsen, P.; Shuba, M. V.; Beckerleg, C.; Yuko, D. I.; Kuzhir, P. P.; Maksimenko, S. A.; Ksenevich, V.; Viet, H.; Nasibulin, A. G.; Tenne, R. *et al.* Influence of Nanotube Length and Density on the Plasmonic Terahertz Response of Single-Walled Carbon Nanotubes. *Journal of Physics D: Applied Physics* **2018**, *51*, 014003.
 48. Kazaoui, S.; Minami, N.; Jacquemin, R.; Kataura, H.; Achiba, Y. Amphoteric doping of single-wall carbon-nanotube thin films as probed by optical absorption spectroscopy. *Physical Review B* **1999**, *60*, 13339–13342.
 49. Jacquemin, R.; Kazaoui, S.; Yu, D.; Hassanien, A.; Minami, N.; Kataura, H.; Achiba, Y. Doping Mechanism in Single-Wall Carbon Nanotubes Studied by Optical Absorption. *Synthetic Metals* **2000**, *115*, 283–287.
 50. Tsapenko, A. P.; Goldt, A. E.; Shulga, E.; Popov, Z. I.; Maslakov, K. I.; Anisimov, A. S.; Sorokin, P. B.; Nasibulin, A. G. Highly Conductive and Transparent Films of H₂AuCl₄-Doped Single-Walled Carbon Nanotubes for Flexible Applications. *Carbon* **2018**, *130*, 448–457.

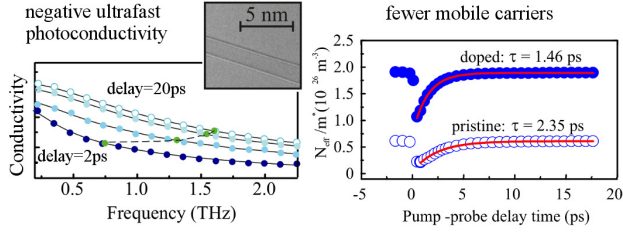
51. Kim, K. K.; Bae, J. J.; Park, H. K.; Kim, S. M.; Geng, H.-Z.; Park, K. A.; Shin, H.-J.; Yoon, S.-M.; Benayad, A.; Choi, J.-Y. *et al.* Fermi Level Engineering of Single-Walled Carbon Nanotubes by AuCl₃ Doping. *Journal of the American Chemical Society* **2008**, *130*, 12757–12761.
52. Yanagi, K.; Okada, R.; Ichinose, Y.; Yomogida, Y.; Katsutani, F.; Gao, W.; Kono, J. Intersubband Plasmons in the Quantum Limit in Gated and Aligned Carbon Nanotubes. *Nature Communications* **2018**, *9*, 1121.
53. Cheung, W.; Patel, M.; Ma, Y.; Chen, Y.; Xie, Q.; Lockard, J. V.; Gao, Y.; He, H. π -Plasmon Absorption of Carbon Nanotubes for the Selective and Sensitive Detection of Fe³⁺ Ions. *Chemical Science* **2016**, *7*, 5192–5199.
54. Kim, S. M.; Kim, K. K.; Jo, Y. W.; Park, M. H.; Chae, S. J.; Duong, D. L.; Yang, C. W.; Kong, J.; Lee, Y. H. Role of Anions in the AuCl₃-Doping of Carbon Nanotubes. *ACS Nano* **2011**, *5*, 1236–1242.
55. Hee Shin, D.; Min Kim, J.; Wook Jang, C.; Hwan Kim, J.; Kim, S.; Choi, S. H. Annealing Effects on the Characteristics of AuCl₃-Doped Graphene. *Journal of Applied Physics* **2013**, *113*, 064305.
56. Joyce, H. J.; Boland, J. L.; Davies, C. L.; Baig, S. A.; Johnston, M. B. A Review of the Electrical Properties of Semiconductor Nanowires: Insights Gained from Terahertz Conductivity spectroscopy. *Semiconductor Science and Technology* **2016**, *31*, 103003.
57. Lu, J.; Liu, H.; Sun, J. Negative Terahertz Photoconductivity in 2D Layered Materials. *Nanotechnology* **2017**, *28*, 464001.
58. Li, X.; Barry, E. A.; Zavada, J. M.; Buongiorno Nardelli, M.; Kim, K. W. Surface Polar Phonon Dominated Electron Transport in Graphene. *Applied Physics Letters* **2010**, *97*, 232105.

59. Scharf, B.; Perebeinos, V.; Fabian, J.; Avouris, P. Effects of Optical and Surface Polar Phonons on the Optical Conductivity of Doped Graphene. *Physical Review B - Condensed Matter and Materials Physics* **2013**, *87*, 035414.
60. Maldague, P. F. Optical Spectrum of a Hubbard Chain. *Physical Review B* **1977**, *16*, 2437–2446.
61. Basov, D. N.; Averitt, R. D.; Van Der Marel, D.; Dressel, M.; Haule, K. Electrodynamics of Correlated Electron Materials. *Reviews of Modern Physics* **2011**, *83*, 471.
62. Georgi, C.; Böhmeler, M.; Qian, H.; Novotny, L.; Hartschuh, A. Probing Exciton Propagation and Quenching in Carbon Nanotubes with Near-Field Optical Microscopy. *Physica Status Solidi (B) Basic Research* **2009**, *4*, 5914–20.
63. Moritsubo, S.; Murai, T.; Shimada, T.; Murakami, Y.; Chiashi, S.; Maruyama, S.; Kato, Y. K. Exciton Diffusion in Air-Suspended Single-Walled Carbon Nanotubes. *Physical Review Letters* **2010**, *104*, 247402.
64. Yoshikawa, K.; Matsuda, K.; Kanemitsu, Y. Exciton Transport in Suspended Single Carbon Nanotubes Studied by Photoluminescence Imaging Spectroscopy. *Journal of Physical Chemistry C* **2010**, *114*, 4353–4356.
65. Yoshida, M.; Popert, A.; Kato, Y. K. Gate-Voltage Induced Trions in Suspended Carbon Nanotubes. *Physical Review B* **2016**, *93*, 041402.
66. Park, J.; Deria, P.; Olivier, J. H.; Therien, M. J. Fluence-Dependent Singlet Exciton Dynamics in Length-Sorted Chirality-Enriched Single-Walled Carbon Nanotubes. *Nano Letters* **2014**, *14*, 504–511.
67. Marulanda, J. M.; Srivastava, A. Carrier density and effective mass calculations in carbon nanotubes. *Physica Status Solidi (B) Basic Research*. 2008; p 9804210.

68. Hertel, T.; Fasel, R.; Moos, G. Charge-Carrier Dynamics in Single-Wall Carbon Nanotube Bundles: A Time-Domain Study. *Applied Physics A: Materials Science and Processing* **2002**, *57*, 449–465.
69. Purewal, M. S.; Hong, B. H.; Ravi, A.; Chandra, B.; Hone, J.; Kim, P. Scaling of Resistance and Electron Mean Free Path of Single-Walled Carbon Nanotubes. *Physical Review Letters* **2007**, *98*, 186808.
70. Nishihara, T.; Okano, M.; Yamada, Y.; Kanemitsu, Y. Review - Photophysics of Trions in Single-Walled Carbon Nanotubes. *ECS Journal of Solid State Science and Technology* **2017**, *6*, M3062.
71. Baig, S. A.; Boland, J. L.; Damry, D. A.; Tan, H. H.; Jagadish, C.; Joyce, H. J.; Johnston, M. B. An Ultrafast Switchable Terahertz Polarization Modulator Based on III-V Semiconductor Nanowires. *Nano Letters* **2017**, *17*, 2603–2610.
72. Docherty, C. J.; Stranks, S. D.; Habisreutinger, S. N.; Joyce, H. J.; Herz, L. M.; Nicholas, R. J.; Johnston, M. B. An Ultrafast Carbon Nanotube Terahertz Polarisation Modulator. *Journal of Applied Physics* **2014**, *115*, 203108.
73. Lui, C. H.; Frenzel, A. J.; Pilon, D. V.; Lee, Y. H.; Ling, X.; Akselrod, G. M.; Kong, J.; Gedik, N. Trion-Induced Negative Photoconductivity in Monolayer MoS₂. *Physical Review Letters* **2014**, *113*, 166801.
74. Mihnev, M. T.; Kadi, F.; Divin, C. J.; Winzer, T.; Lee, S.; Liu, C. H.; Zhong, Z.; Berger, C.; De Heer, W. A.; Malic, E. *et al.* Microscopic Origins of the Terahertz Carrier Relaxation and Cooling Dynamics in Graphene. *Nature Communications* **2016**, *7*, 11617.
75. Tomadin, A.; Horneett, S. M.; Wang, H. I.; Alexeev, E. M.; Candini, A.; Coletti, C.; Turchinovich, D.; Kläui, M.; Bonn, M.; Koppens, F. H. *et al.* The ultrafast dynamics and conductivity of photoexcited graphene at different Fermi energies. *Science Advances* **2018**, *4*, 5313.

76. Eklund, P. C.; Holden, J. M.; Jishi, R. A. Vibrational Modes of Carbon Nanotubes; Spectroscopy and Theory. *Carbon* **1995**, *33*, 959–972.
77. Monti, M.; Tao, S. X.; Staniforth, M.; Crocker, A.; Griffin, E.; Wijesekara, A.; Hatton, R. A.; Lloyd-Hughes, J. Efficient Intraband Hot Carrier Relaxation in the Perovskite Semiconductor $\text{Cs}_{1-x}\text{Rb}_x\text{SnI}_3$ Mediated by Strong Electron-Phonon Coupling. *Journal of Physical Chemistry C* **2018**, *122*, 20669–20675.

For Table of Contents Use Only



Giant negative terahertz photoconductivity in controllably doped carbon nanotube networks

M. G. Burdanova, A. P. Tsapenko, D. A. Satco, R. Kashtiban, C. D. W. Mosley, M. Monti, M. Staniforth, J. Sloan, Y. G. Gladush, A. G. Nasibulin and J. Lloyd-Hughes.

Synopsis: Carbon nanotube thin films were shown to exhibit large negative photoconductivity, where the conductivity lowered after optical excitation, before recovering on picosecond timescales (left). The reduction and recovery of the mobile carrier density (right) was tracked using ultrafast terahertz spectroscopy. The large modulation depth, and tunability of the recovery time with doping (right), offers promise for ultrafast devices including THz detectors, polarizers and modulators.

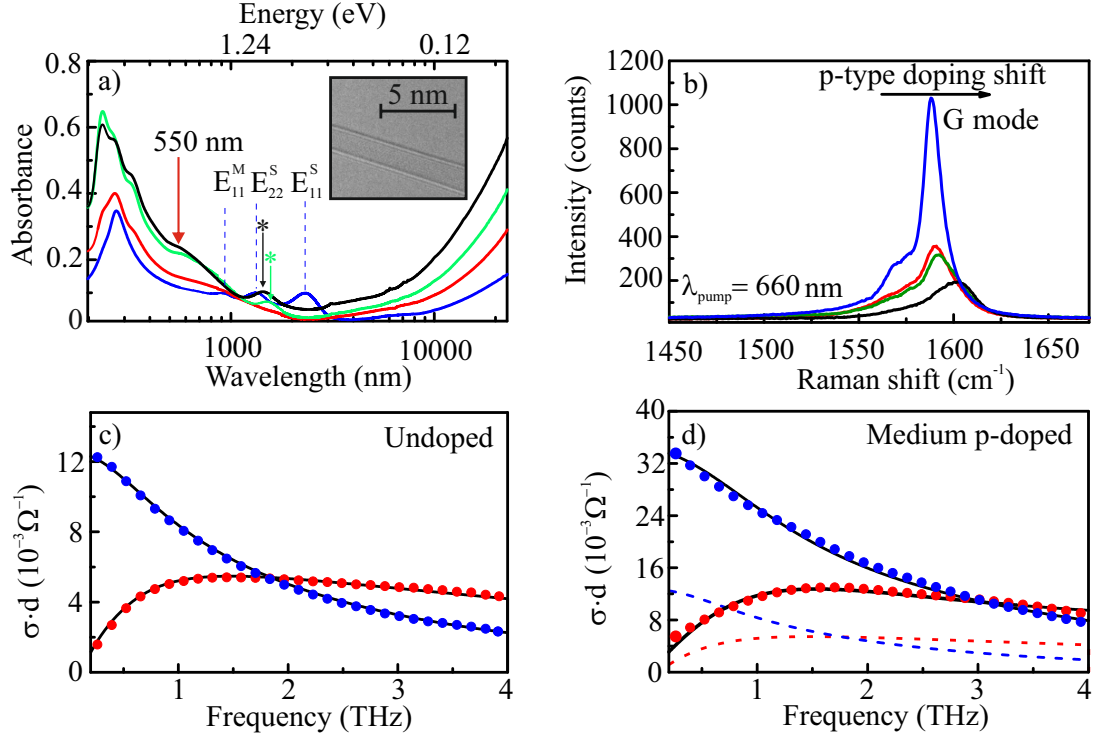


Figure 1: The transmittance (a) and Raman (b) spectra of pristine (blue) and chemically-doped SWCNTs made from HAuCl_4 solutions with concentrations 4 mM (red), 15 mM (green) and 30 mM (black). The red arrow indicates the surface plasmon mode of the adsorbed gold nanoparticles around 550 nm, while the black and green arrows with asterisks mark the positions of intersubband plasmons. The insert shows a typical TEM image of a single SWCNT. (c) Equilibrium sheet conductivity of a pristine SWCNT film. (d) Equilibrium sheet conductivity of a film doped by 15 mM HAuCl_4 . The real (blue circles) and imaginary (red circles) parts of the measured conductivity are fit by the combined Drude and plasmon model (solid lines). The dashed line shows the pristine sample's sheet conductivity for comparison.

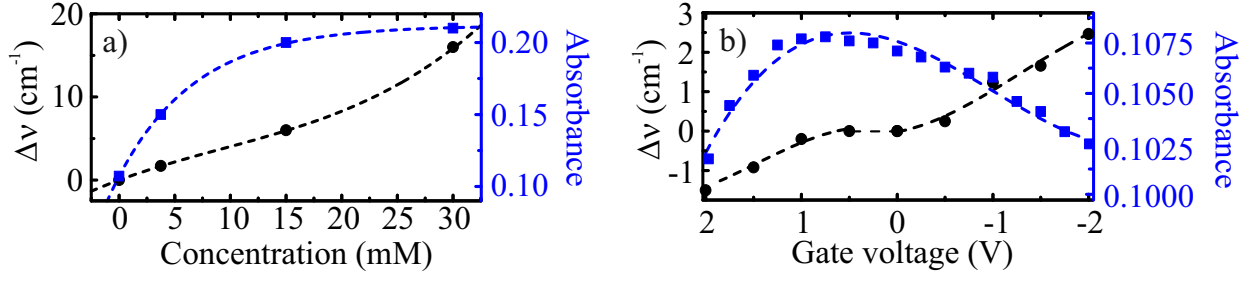


Figure 2: The change in G⁺ mode position at 660 nm and absorbance at 650 nm for (a) adsorption doped samples as a function of the dopant concentration and (b) electrically-gated sample as a function of applied voltage. The axis for voltage was reversed to show the similar trend of Raman shift for doped and negatively biased samples. The solid lines are guides for the eye.

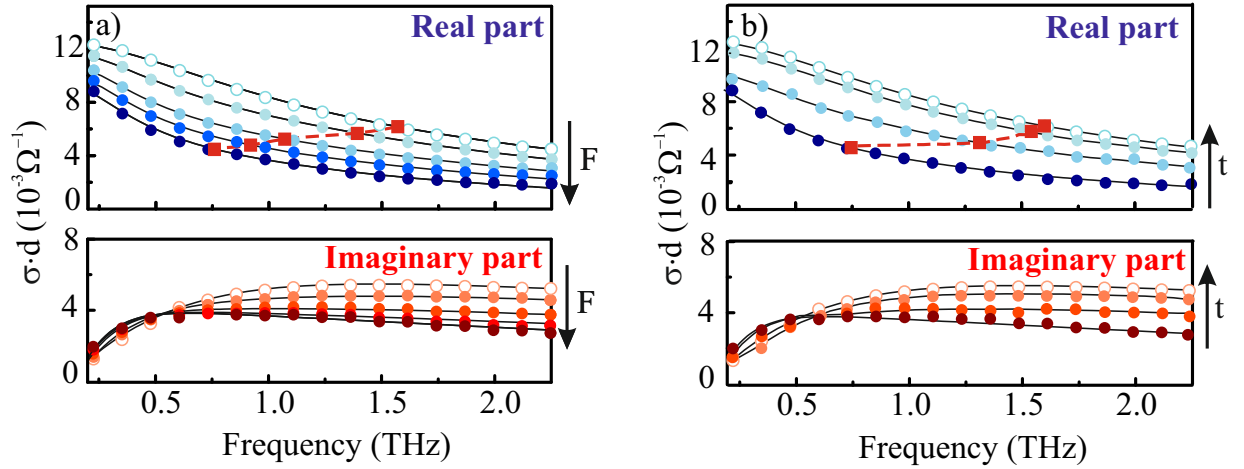


Figure 3: (a) Equilibrium conductivity (empty dots) and conductivity at $t = 2$ ps after excitation (filled dots) of the pristine SWCNT film at fluence $F = 0, 2.8, 6.95, 14.3, 26 \mu\text{J}/\text{cm}^{-2}$. Real (blue circles) and imaginary (red circles) parts of the measured sheet conductivity (σd) are plotted. The arrow points from low to high fluence. The red squares and dashed line mark the change in f_{HWHM} . (b) Conductivity at $t = 1.8$ ps, 3.2 ps, 5.4 ps and 20 ps after photoexcitation, for $F = 26 \mu\text{J}/\text{cm}^{-2}$. The arrow points from early to later times.

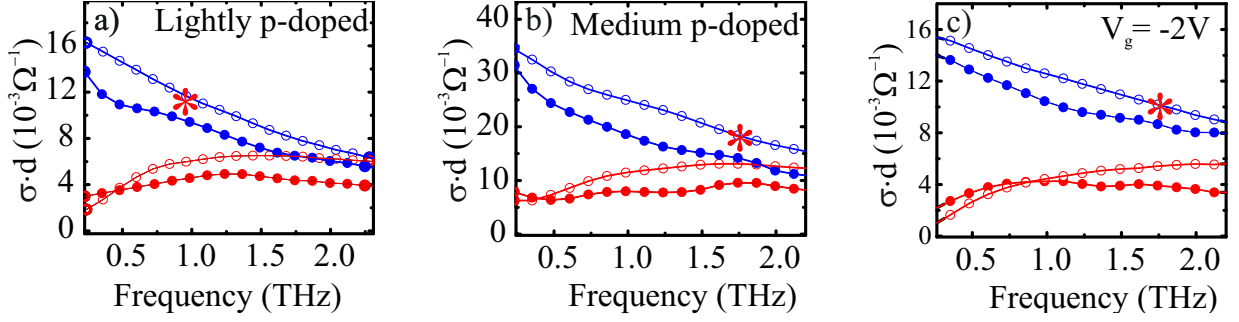


Figure 4: Equilibrium conductivity (empty dots) and conductivity 2 ps after photoexcitation at $F = 26 \mu\text{Jcm}^{-2}$ (filled dots) of (a) film doped with 4 mM HAuCl_4 ; (b) film doped with 15 mM HAuCl_4 ; (c) ionically gated sample at $V_g = -2.0$ V. Real (blue circles) and imaginary (red circles) parts of the measured conductivity are plotted. The red asterisks indicate the position of weak additional peaks present after doping.

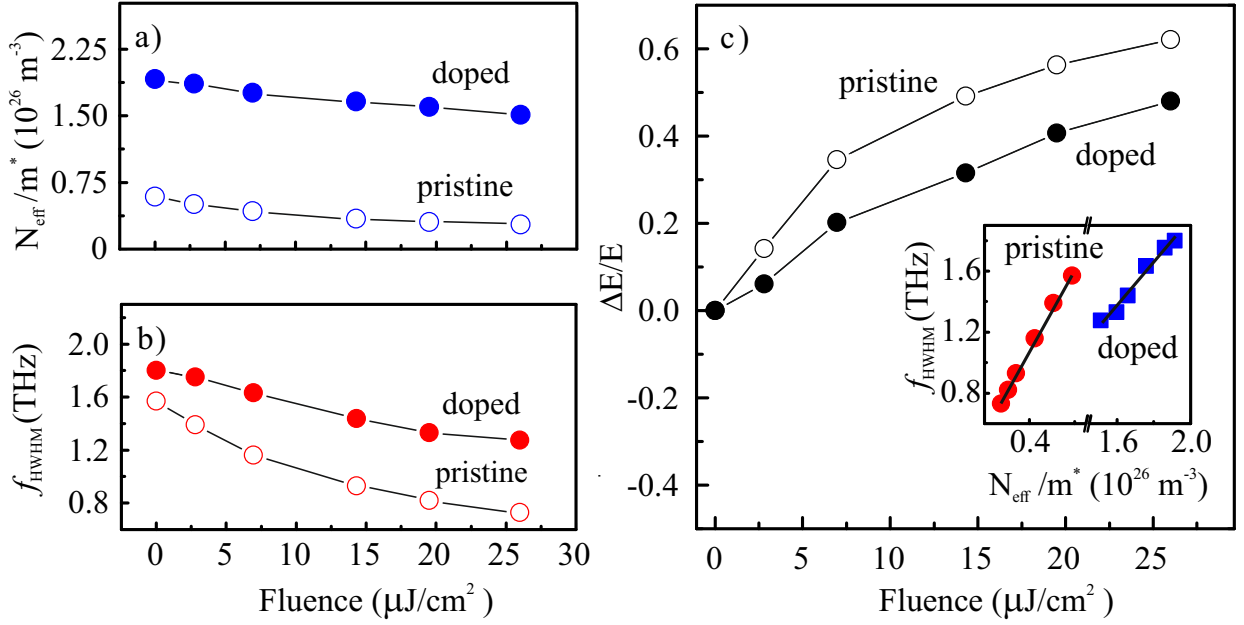


Figure 5: (a) Ratio of effective density of electrons to effective mass, N_{eff}/m^* , versus fluence, F , for pristine (open circles) and 15 mM doped sample at $t = 2$ ps (filled circles). (b) Frequency width of $\sigma_1(\omega, t = 2 \text{ ps})$, f_{HWHM} , versus F . (c) $\Delta E/E$ at the peak of the THz pulse and pump-probe delay $t = 2$ ps. The insert shows the linear dependence between f_{HWHM} and N_{eff}/m^* .

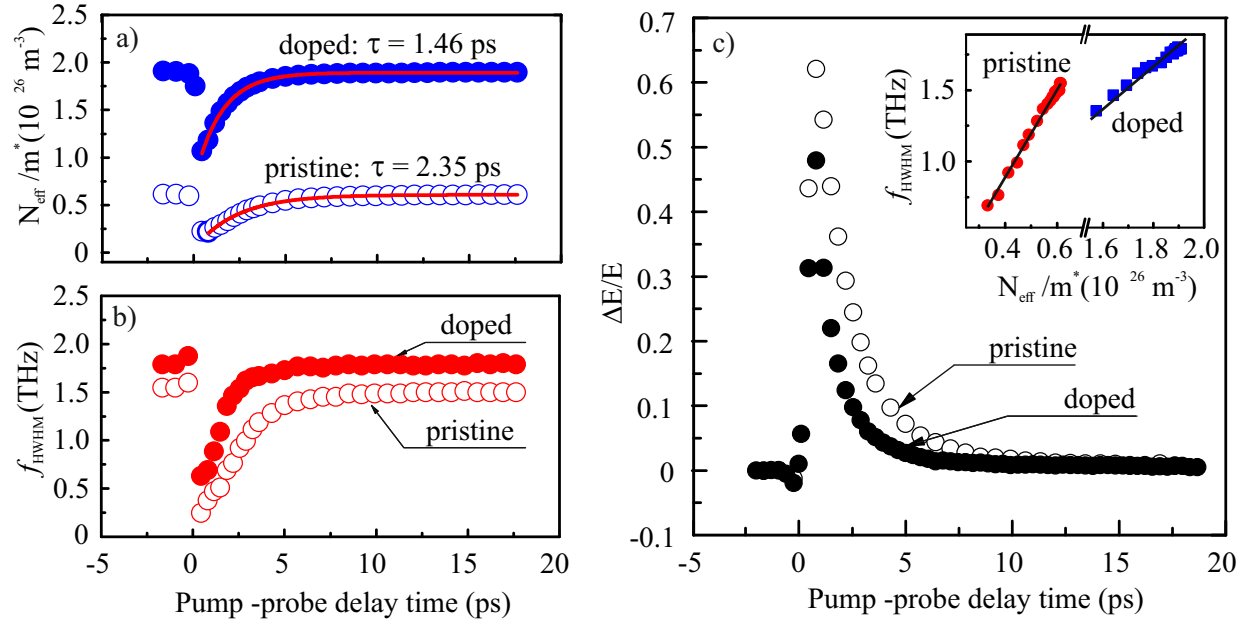


Figure 6: (a) Ratio of effective density of electrons to effective mass, N_{eff}/m^* , versus pump-probe delay time t for pristine (open circles) and 15 mM doped (filled circles) samples. (b) Frequency width of $\sigma_1(\omega, t)$, f_{HWHM} , versus t . (c) $\Delta E/E$ at the peak of the THz pulse versus t . The insert shows the linear dependence between f_{HWHM} and N_{eff}/m^* .